Proceedings of the Thirty-sixth (2026) International Ocean and Polar Engineering Conference **www.isope.org**
Orlando, Florida, USA, May 31-June 5, 2026

ISBN 978-1-880653-72-2; ISSN 1098-6189

Numerical Study on the Effect of Bow Rake Angle on Green Water Phenomena of the KCS Ship

Yuxuan Xu[1], Xi Chen[2], Ganghui Liu[2], Yuan Zhuang[1], Jianhua Wang[1], Decheng Wan[1]*

[1] Computational Marine Hydrodynamics Lab (CMHL), School of Ocean and Civil Engineering,
Shanghai Jiao Tong University, Shanghai, China
[2] China Ship Development and Design Center, Shanghai, China
[*]Corresponding Author

ABSTRACT

Green water occurrence is a highly nonlinear hydrodynamic phenomenon commonly observed during medium- to high-speed head-sea navigation. The transient impact pressure induced by green water can significantly affect the local strength and durability of the hull, as well as cause damage to the deck and superstructure. The bow geometry, particularly the bow rake angle, plays a crucial role in determining the frequency and intensity of green water events. However, quantitative investigations into the influence of rake angle variations remain limited. In this study, the KCS containership is adopted as the research object. The bow region is parametrically deformed using the Non-Uniform Rational B-Splines (NURBS) method to generate a series of hull forms with different rake angles. The viscous flow solver naoe-FOAM-os is employed to numerically simulate the green water phenomena of these hull variants under regular head-wave conditions, yielding detailed results of local peak pressures and flow field evolution. By comparing the green water responses among different rake configurations, the influence mechanism of bow rake angle on green water intensity and occurrence is elucidated. The findings provide theoretical reference and engineering guidance for bow form optimization, anti-green-water structural design, and prediction of green water loads.

KEY WORDS: Green Water Phenomena; KCS; bow rake angle; slamming; naoe-FOAM-os.

INTRODUCTION

Green water is a strongly nonlinear hydrodynamic event that occurs when a ship at moderate-to-high speed meets large or steep waves. It involves free-surface plunging, jetting and splashing, air entrainment, and short-duration high impact loads. These events produce localized high stresses that can damage structure and threaten safety. Accurately describing how green water starts, evolves, and applies loads is therefore important for design, durability assessment, and risk control.

Container ships normally operate at relatively high speed. This makes them more vulnerable to green-water events in large seas. Key factors that affect green water include vessel speed, encounter angle, wave spectrum, and bow geometry. Prior studies indicate that peak pressures induced by green water generally increase with ship speed. And some studies show that bow geometry changes can reduce or change the impact pattern and intensity. Kudupudi et al. (2023) investigated the effects of factors which impact green water events and peak pressure on ship decks using Computational Fluid Dynamics (CFD) methods. They concluded that peak pressure caused by wave surges increases significantly with ship speed but decreases with increased bow angle.

To more accurately investigate these influencing mechanisms, researchers employed multiple methods to conduct simulation studies. Some researchers employ high-fidelity two-phase flow simulations to directly analyze details such as free-surface evolution, jet flow, and air entrainment. Gatin et al. (2018) conducted numerical simulations about green water using open-source CFD computational software. They also validated the accuracy of CFD methods in capturing green water through experimental comparisons. Liu et al. (2022) constructed a 3D numerical tank to investigate wave conditions on the ship's bow under deformed wave. They summarized the distribution characteristics of primary impact points across different hull regions. Some researchers use potential-viscous flow coupling methods to approach captures green-water phenomena while reducing computational cost. Jiao et al. (2021) combined CFD and Finite Element Analysis (FEA) to simulate wave loads and green water slamming pressures on an elastic S175 container ship under different regular waves. Zhang et al. (2023) used a CFD–FEA coupling method to compute impact loads and the structural response of the bow under deformed waves. Their results show that green water can impart large impacts on the bow deck, induce severe structural responses, and potentially cause damage. Lee et al. (2012) performed towing tank tests on an FPSO model to investigate how three different bow shapes affect green-water behavior under regular waves.

Studies have systematically shown how factors such as the hull's bow slamming and speed affect green water phenomena. They find that increases in wave height and ship speed generally amplify green water height and wave steepness, and promote plunging-type breaking. However, few studies have treated the ship's bow rake angle as an independent variable and examined its effect on bow green water morphology and loading under controlled conditions of identical speed and sea state.

This paper focuses on the KCS hull. We apply the free-form deformation (FFD) method to vary its bow rake angle. Under representative high speed and large wave steepness conditions, we perform simulations using the Volume of Fluid (VOF) method coupled with Delayed Detached Eddy Simulation (DDES) to analyze green water formation mechanisms and to investigate the effect of bow rake angle on green water morphology and deck impact loads. During the simulation process, the HOS method was coupled with CFD method. We used HOS method to generate a fully developed external wave field, leveraging its high efficiency in wave generation. Then overset mesh technique the self-developed naoe-FOAM-os solver (Zhirong Shen, 2016) was combined to solve the motion response of the KCS vessel and flow field information in the viscous inner domain near the hull.

METHODOLOGY

Governing Equation

In this paper, the Delayed Detached Eddy Simulation (DDES) method is employed for numerical simulation. Compared to the DES method, DDES (SPALART P R, 2006) introduces a delay function to reconstruct the length scale. Simultaneously, it considers the grid scale and the vortex-viscoelastic field, which prevents the transition from Reynolds Average Navier-Stokes (RANS) to Large Eddy Simulation (LES) from occurring too close to the wall surface and avoids premature separation in the model prediction. Based on the SST model, the control equation of DDES is defined as follows:

$$\frac{\partial \rho k}{\partial t} + \nabla \cdot (\rho \mathbf{U} k) = \nabla \cdot \left[(\mu + \sigma_k \mu_t) \nabla k \right] + P_k - \rho \frac{\sqrt{k^3}}{l_{DDES}} \tag{1}$$

$$\begin{aligned} \frac{\partial \rho \omega}{\partial t} + \nabla \cdot (\rho \mathbf{U} \omega) = \nabla \cdot \left[(\mu + \sigma_\omega \mu_t) \nabla \omega \right] + \\ 2(1 - F_1) \rho \sigma_{\omega 2} \frac{\nabla k \cdot \nabla \omega}{\omega} + \alpha \frac{\rho}{\mu_t} - \beta \rho \omega^2 \end{aligned} \tag{2}$$

$$\mu_t = \rho \frac{a_1 k}{\max(a_1 \omega, F_2 S)} \tag{3}$$

where, ρ is the fluid density; $\mathbf{U}$ is the velocity; k is the turbulent kinetic energy; l_{DDES} is the DDES length scale; ω is the specific dissipation rate; σ_k=0.85, σ_ω=0.5, $\sigma_{\omega 2}$=0.856, a_1=0.31, α=1, β=0.09, they are all model coefficients; S is the strain-rate tensor; P_k is production terms; P is pressure; μ_t is the turbulent viscosity; F_1 and F_2 are the SST blending functions.

In Eq. 1 the DDES length scale l_{DDES} is defined as below.

$$l_{DDES} = l_{RANS} - f_d \max(0, l_{RANS} - l_{LES}) \tag{4}$$

where, l_{RANS} and l_{LES} are the RANS and LES length scales.

The length scale of DDES is related to the vortex viscosity field and time, enabling RANS models to exhibit self-sustaining functionality. If the mathematical function f_d indicates a point lies within the boundary layer, the model using the length scale l_{DDES} can transition to the LES model. When large scale separated flow occurs, the value of f_d changes from 0 to the LES model. Following fluid separation, the transition from RANS to LES occurs more rapidly than with DES methods. DES combines the advantages of RANS and LES while reducing computational load compared to LES. DDES addresses the gray zones and insufficient modal stresses existing in DES.

High-Order Spectral (HOS) Method

The High-Order Spectral (HOS) method is based on the pseudo-spectral approach and the Fast Fourier Transform (FFT). It was proposed in 1987 by West et al. (1987) and Dommermuth et al. (1987). The method solves inviscid, incompressible flow where the velocity potentiala $\phi(x, y, z, t)$ satisfies Laplace's equation. Let the free-surface elevation be $z = \eta(x, y, t)$. The free-surface velocity potential $\phi^s(x, y, t)$ can be written as:

$$\phi^s(x, y, t) = \phi\big(x, y, \eta(x, y, t), t\big) \tag{5}$$

where, ϕ is the velocity potential; ϕ^s is the velocity potential at the horizontal surface; t is time, x and y are grid points within the fluid domain; η is the wave surface elevation function with respect to x, y and t.

In the HOS method, the velocity potential ϕ is perturbatively expanded into an M^{th} order series (Zakharov, 1972), yielding:

$$\phi(x, y, z, t) = \sum_{m=1}^{M} \phi^{(m)}(x, y, z, t) \tag{6}$$

Then each order component $\phi^{(m)}$ is Taylor-expanded about $z = 0$ on the free surface and retained up to order M - m. Thus:

$$\phi^s(x, y, t) = \phi(x, y, \eta, t) = \sum_{m=1}^{M} \sum_{k=0}^{M-m} \frac{\eta^k}{k!} \frac{\partial^k}{\partial z^k} \phi^{(m)}(x, y, 0, t) \tag{7}$$

Given ϕ^s and η at time t and appropriate boundary conditions, one can solve for their values at the next time step. By solving a sequence of boundary-value problems for $\phi^{(m)}$, the time evolution of the free-surface wave field is obtained.

Viscous-Potential Flow Coupling Model

Based on the HOS method, the wave field data generated by HOS-NWT are fed into the inner-domain wave field of waves2Foam through a relaxation zone. However, the solution of the ship motion in the inner domain does not affect the evolution of waves in the outer domain. A one-way coupled solver is constructed in Waves2Foam following Jacobsen et al. (2012). The relaxation scheme in the relaxation zone is:

$$\alpha = (1 - \chi)\alpha_c + \chi \alpha_t \tag{8}$$

$$\mathbf{u} = (1 - \chi)\mathbf{u}_c + \chi \mathbf{u}_t \tag{9}$$

where, α_c and $\mathbf{u}_c$ are the volume fraction and velocity obtained from the viscous solver, and α_t and $\mathbf{u}_t$ are the volume fraction and velocity from the potential-flow solver. The weighting coefficient χ is defined as:

$$\chi(\xi) = 1 - \frac{\exp\left(\xi^{\beta}\right) - 1}{e - 1} \tag{10}$$

where, β is a parameter, typically taken as 3.5; ξ is the local coordinate in the transverse direction (with values in [0,1]), taking value 0 at the interface to the outer wave field and value 1 at the interface to the inner wave field.

The computational domain and relaxation-zone arrangement for the two-dimensional one-way coupling model are shown in Fig. 1. Through the relaxation zone, HOS potential-flow data are injected as the wave-generation boundary condition for the CFD domain.

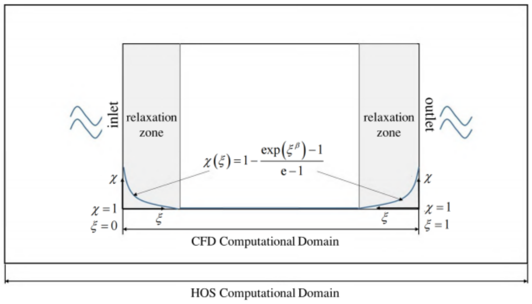

Fig. 1 Computational Domain and relaxation zone

Overset Mesh Method

When solving for hull motion in waves, an overset mesh method is required to ensure the accuracy and stability of numerical solutions for large-amplitude motion responses under resonance conditions.

The overset mesh method is used to generate meshes for the entire flow-field computational domain and the moving ship body separately. The whole computational domain is therefore divided into two parts: a background mesh and a body-fitted mesh containing the ship. These two meshes overlap in certain regions, and interpolation relationships are established through the SUGGAR++ program to exchange flow-field information, referred to as domain connectivity information (DCI).In this paper, the overset mesh method is implemented based on the self-developed naoe-FOAM-os solver (Zhuang, 2021).

NUMERICAL SETUP

Numerical Model

Fig. 2 Geometry of KCS ship model

The KCS ship is the standard ship model adopted in the Tokyo 2015 CFD Workshop and is also a widely studied container ship among scholars. The geometry of KCS model is shown in the Fig. 2.

The numerical calculations in this paper employ a KCS model with a length of 6.0702 m and the scaling ratio $\lambda = 37.9$. Its fundamental parameters are shown in Table 1.

Table 1. Main particulars of KCS model

Particulars	Actual scale	Model scale
Length between perpendiculars, L_{pp}	232.5 m	6.0702 m
Breadth at waterline, B_{WL}	32.2 m	0.8498 m
Draft, T	10.8 m	0.2850 m
Displacement volume, ∇	52030 m^3	0.9571 m^3
Wetted surface area, S	9424 m^2	6.6177 m^2
Longitudinal center of buoyancy, $\frac{LCB}{L_{pp}}$	-1.48	-1.48
Vertical center of gravity, VCG	-	0.093

Computational domain and mesh

The computational domain is illustrated in Fig. 3, with dimensions of -1.5L_{pp} to 3.5L_{pp} in length, -L_{pp} to L_{pp} in width, and -L_{pp} to 0.5L_{pp} in height. The top boundary and the bottom boundary is set as a slip condition, and the left and right sides are defined by symmetry boundary conditions.

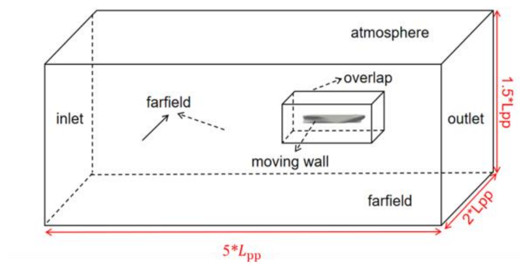

Fig. 3 CFD Computational domain

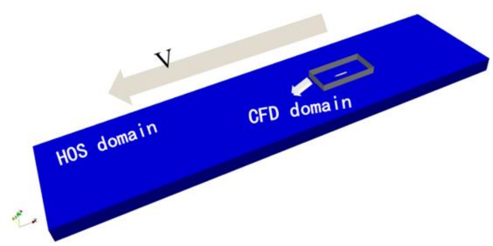

Fig. 4 Relative position of the CFD domain within the HOS domain

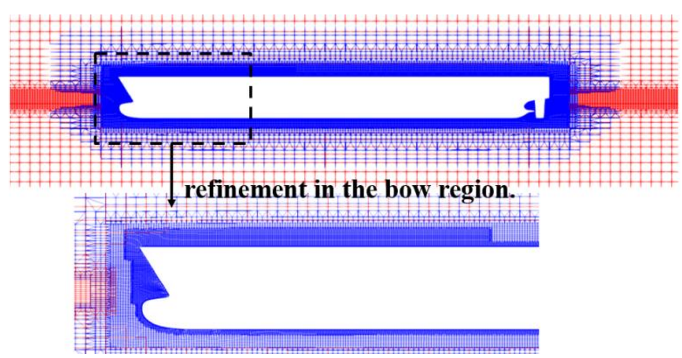

Fig. 5 Computational meshes in XY plane

Due to the overset mesh method, the figure shows two distinct mesh sets: the background mesh and the hull mesh, totaling approximately 13.53 million. To control the number of mesh, the background mesh was generated by setting "simpleGrading" in the blockMeshDict file. This ensures uniform distribution of the hull region mesh in the x, y and z directions, while the mesh in the surrounding areas transitions gradually from larger to smaller sizes toward the hull region. To accurately capture green water and prevent numerical dissipation, the free surface was first refined. Mesh refinement was applied around the hull perimeter, followed by further refinement in the bow region.

Condition parameter setting

To investigate the effect of bow rake angle on green water event, the bow rake angle of the KCS ship was altered using a FFD method, changing inward and outward by ten degrees respectively. The contours of the deformed bows in the XY plane are shown in Fig. 7:

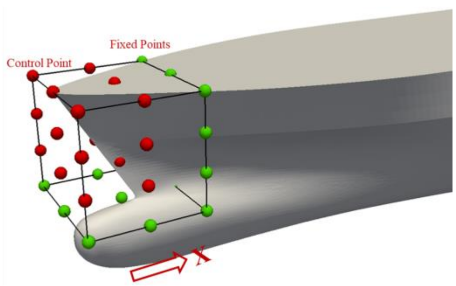

Fig. 6 Moving lattice control points to deform KCS ship (FFD)

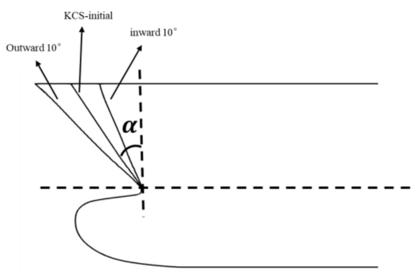

Fig. 7 The contours of the deformed bows in the XY plane

Case 0 is used to validate the accuracy of the solution method and results. Here, the regular wave parameters and ship speed are set identical to the experiment. The calculated results for heave and pitch motion curves are compared with the experimental findings. Specifically, following the research by 2015 Tokyo Workshop, we set the wavelength-to-ship length ratio to 1.15, the wave steepness to 0.0167, and the ship speed to $F_r = 0.26$.

Table 2. Specifications for simulation cases

Margins	Model	Wavelength -to-ship length ratio	Wave steepness	Ship speed (Fr)
Case0	KCS-initial	1.15	0.0167	0.26
Case1	KCS-initial	1.15	0.025	0.26
Case2	outward 10^o	1.15	0.025	0.26
Case3	inward 10^o	1.15	0.025	0.26

In cases 1 through 3, to induce green water event, the wavelength-to-ship-length ratio of the regular waves was maintained at 1.15 and the ship speed is maintained at $F_r = 0.26$, but the wave steepness was increased to 0.025. The calculations employ the initial KCS model, a KCS hull form with the bow rake angle deflected outward by 10^o, and a KCS hull form with the bow direction altered inward by 10^o.

VERIFICATION AND VALIDATION

Experimental comparison and validation

To ensure the reliability and accuracy of our simulation, we selected case 0 for comparative validation. We employed HOS-NWT to generate waves within the HOS domain. By setting measurement points at the ship's initial coordinate origin, we observed the wave height time history curve at this location within the HOS domain. The corresponding wave time history curve for the HOS field is shown below:

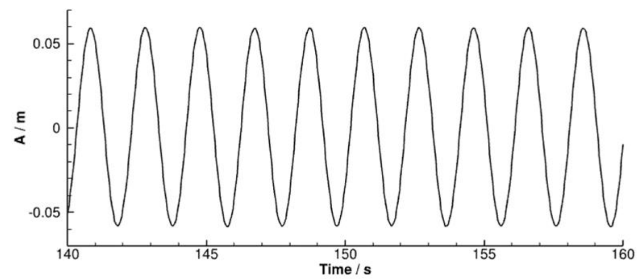

Fig. 8 regular wave for case0

Simulation calculations were performed on the KCS ship using the HOS-CFD coupling method. The resulting ship heave and pitch motion curves were compared with reference data, as shown below:

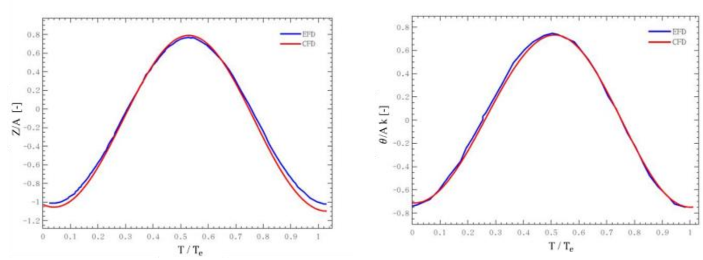

(a) Heave (b) Pitch

Fig. 9 Heave and pitch motion comparison curves

Fig. 9(a) shows the non-dimensionalized time on the horizontal axis and the non-dimensionalized heave motion value on the vertical axis. Fig. 9(b) shows the non-dimensionalized time on the horizontal axis and the non-dimensionalized pitch motion value on the vertical axis. As evident from Fig. 9, the simulated KCS ship's heave and pitch motion curves exhibit periods consistent with experimental results. Although the simulated heave troughs are slightly larger than those observed experimentally, the error remains within an acceptable range. Comparison with experimental data validates the accuracy of the simulation calculations.

RESULTS AND DISSCUSSIONS

Green water phenomenon

In case 1, we performed simulation calculations on the original KCS ship model and analyzed the green water phenomenon. Before the calculations, we first generated regular waves within the HOS domain using HOS-NWT. By setting measurement points at the ship's initial coordinate origin, we observed the wave height at that location within the HOS domain. The corresponding HOS field wave time history curve is shown in Fig. 10:

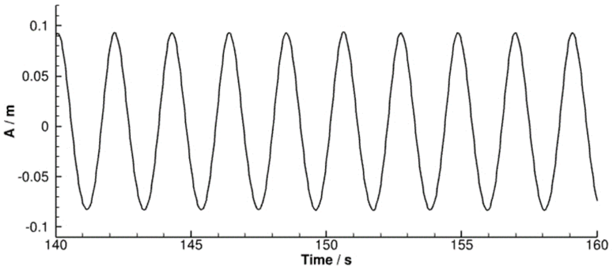

Fig. 10 regular wave for case1-3

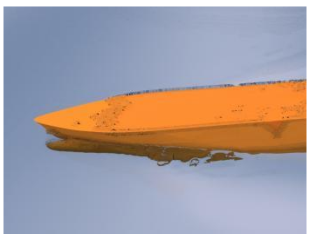

(a) T=0

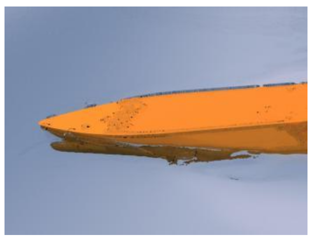

(b) T=2

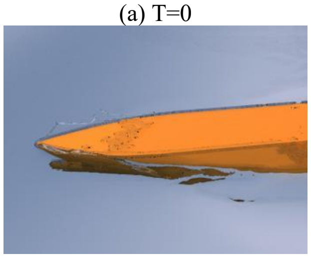

(c) T=3

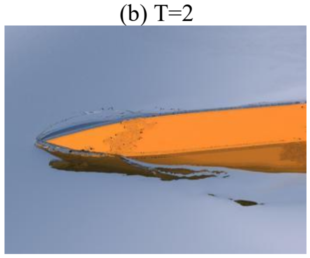

(d) T=4

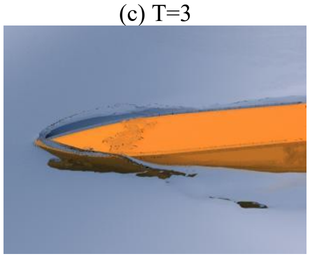

(e) T=5

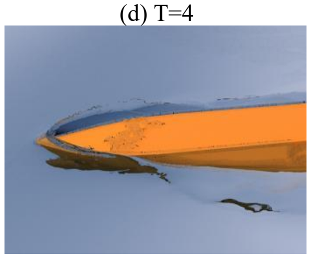

(f) T=6

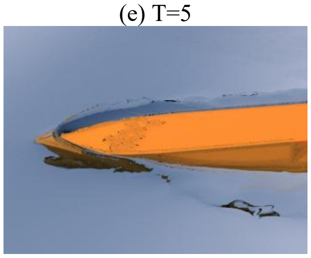

(g) T=7

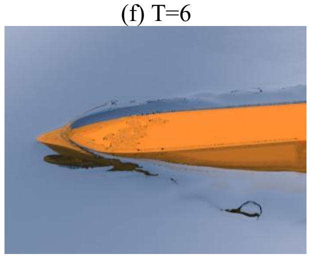

(h) T=8

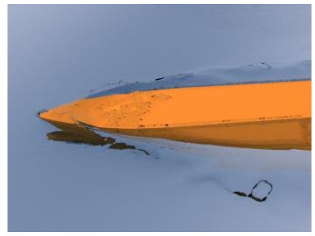

(i) T=9

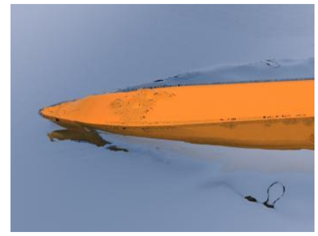

(j) T=10

Fig. 11 Green water occurrence phenomena in case1

Fig. 11 presents a sequence of pictures that illustrate the bow green-water process observed on the KCS model. When the incident wave interacts with the hull sides, the free surface first climbs along the hull and produces a local thickening of the wave crest ahead of the bow. Prior to reaching deck level, this front commonly exhibits partial breaking and surface fragmentation. Upon arrival at deck height, a portion of the flow with high kinetic energy is expelled both upward and outward as jets. As the bow submerges further, the overtopping flow intrudes onto the deck and develops into a tongue-shaped sheet. This is immediately followed by additional inflow from the surrounding free surface that rapidly floods the forward deck region. Under conditions of high forward speed, the deck impact assumes the character of a plunging wave and the event can be described by a classic plunging-dam-break (PDB) type collapse.

If superstructures exist, significant impact and splashback can be anticipated (this KCS model lacks superstructures). After the initial plunging and overtopping, a large volume of water accumulates at the bow and subsequently disperses laterally and aft under the influence of the ship's forward motion and flow recirculation. The sequence therefore comprises run-up, localized breaking, jetting and tongue formation, PDB-type plunging impact, and post-impact pooling and dispersion. All processes together govern the magnitude and time history of impulsive deck pressures and the subsequent structural and operational consequences.

Fig. 12 presents the dynamic pressure distributions on the fore deck during the green water events corresponding to Fig. 11(f) - Fig. 11(h). As shown, the overtopping water rapidly converges onto the deck from multiple directions around the bow, forming an elongated tongue-shaped region of elevated pressure that propagates aft and subsequently spreads laterally. This pressure pattern is fully consistent with the observed free-surface evolution and confirms that the green water intrudes onto the deck in a coherent tongue-like form before dispersing.

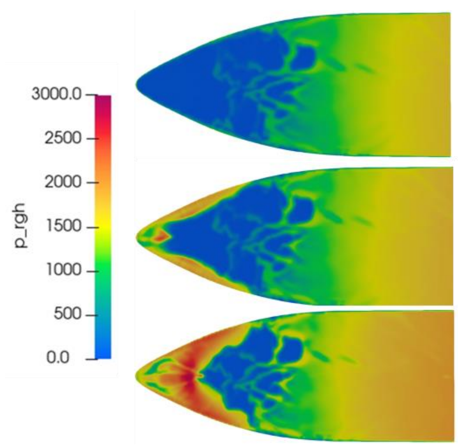

Fig. 12 Dynamic pressure on the bow deck

A notable feature is that the highest pressures do not occur at the foremost point of the bow. Instead, the pressure maxima are located slightly aft of the stem and offset to either side of the centerline on the forward deck. This indicates that, during plunging-type green water events, the high-momentum jet does not directly impinge on the bow tip; rather, it undergoes strong normal deceleration and momentum dissipation on the forward deck, where localized pressure amplification takes place. Such a distribution is characteristic of a classic plunging-dam-break (PDB) type collapse, in which the high-speed jet formed during the run-up and jetting stages plunges onto the deck and generates intense impulsive loads downstream of the stem.

Pressure sensors (probes) were installed in the bow region and on the fore deck as shown in Fig. 13. Probes labeled 0 through 4 were mounted on the stem at equal elevations, with Probe 4 located at deck level. Four additional probes were mounted on the hull sides at elevations corresponding to those of Probes 1 and 2. Five probes were installed across the deck at equal spacing.

Fig. 13 Probes distribution in case 1

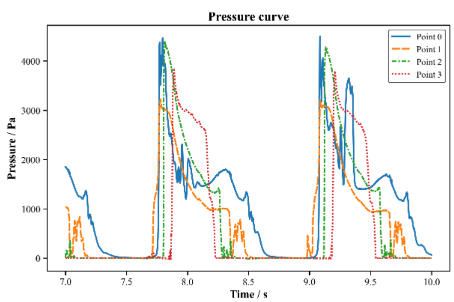

(a) Pressure curves of points 0-4

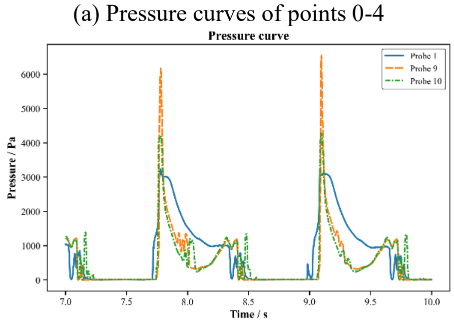

(b) Pressure curves of points 1,9,10

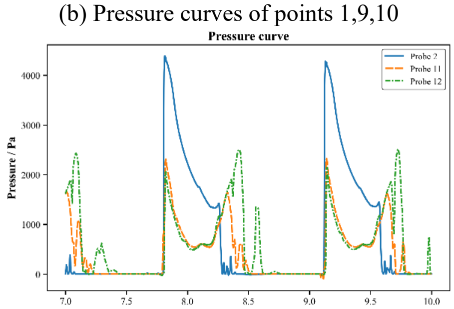

(c) Pressure curves of points 2,11,12

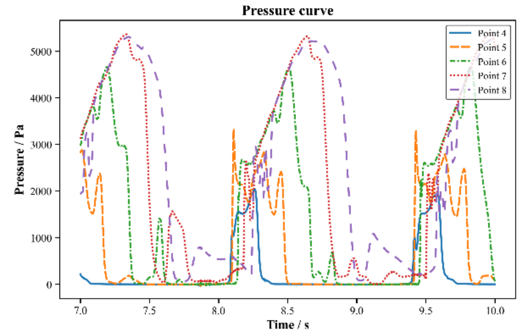

(d) Pressure curves of points 4-8

Fig. 14 Pressure curves of probes in case 1

By combining the free surface with the probe time histories, we directly map pressure signatures to distinct stages of the green water event. In time, side-hull and low-stem probes respond first, showing short, steep pressure rises. This response matches the run-up along the hull sides and the local convergence at the bow seen in the animations. Next, probes at the elevations of Probe-1 and Probe-2 record sharper transient peaks. These peaks coincide with the transition from run-up to local breaking/jetting and indicate strong normal deceleration of the post-breaking jets at those elevation planes. Only after overtopping do the deck probes show dominant responses. Deck pressures change from narrow spikes to broader high-pressure plateaus, consistent with the formation of a tongue-shaped inundation, its plunging onto the deck, and subsequent pooling at the forward deck. Some deck probes register instantaneous peaks that exceed 5 kPa; however, the longer duration of the deck loads means the resulting impulse can match or exceed the effect of shorter, higher peaks.

Spatially, the largest instantaneous peaks do not always occur at the bow tip. They frequently appear at side-hull locations or on the forward deck, in agreement with the observed impact position of the tongue leading edge. In summary, the pressure and free-surface data together characterize the sequence: lateral run-up→local breaking/jetting→plunging/tongue formation→deck pooling and spread. The side run-up supplies the initial momentum and short impulses; mid-height breaking/jetting produces the strongest transient impacts; the deck region sustains retained loads with significant impulse.

Effects of different rake angles

To evaluate the influence of the rake angle on the green water event, we performed identical post-processing on the flow fields of case2 and case3. The free surface, instantaneous pressure field, and pressure time histories at several representative measurement points were then compared side-by-side with case1. First, the comparison of the free surface.

Fig. 15 shows that larger rake angles promote earlier onset of wave overturning and breaking on the side hull. Conversely, with smaller heel the side run-up develops more slowly, and the free surface tends to accumulate more mass ahead of the bow before overtopping. The resulting larger tongue-shaped inundation transports a greater water volume onto the fore deck due to longer retention.

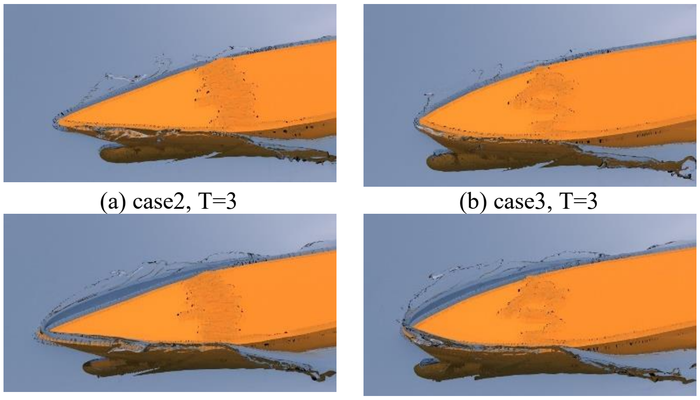

(a) case2, T=3 (b) case3, T=3

(c) case2, T=4 (d) case3, T=4

Fig. 15 Free surface of two cases (time is same as Fig. 11(c) and (d))

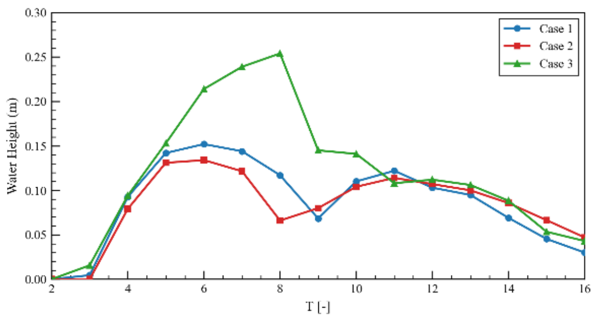

Fig. 16 The time histories of green-water elevation

Fig. 16 shows the time histories of green-water elevation referenced to the deck baseline for the three heel-angle cases. The picture shows that all three rake angle cases follow the same overall overtopping sequence: rapid growth, peak, and decay. The cases differ mainly in peak magnitude and persistence. The smaller rake angle case attains higher deck elevations and sustains them for longer, while the middle and large cases show lower peaks and more rapid decay. Thus, rake angle does not substantially change the onset of overtopping but modifies accumulation and retention on the deck. A reduced rake angle promotes pooling and longer-lasting deck loading; an increased rake angle tends to suppress retention and produce briefer overtopping events.

To validate the foregoing conclusions, we extracted pressure time histories at representative probe locations on the model and compared the responses between case 2 and case 3. The probe layout and numbering are shown in Fig. 17.

Fig. 18 presents time-history comparisons of pressure at the same relative location on the side hull for different heel angles (case 1: probe 11, case 2: probe 12, case 3: probe 11). The three cases show similar peak levels during the initial impact, indicating that the first arrival of the wave produces comparable loading at this location regardless of rake angle. In contrast, the secondary impact displays a clear dependence on rake angle: the secondary peaks increase in magnitude with larger rake angles, with case2 exhibiting higher secondary peaks than case1 and case 3.
This result is consistent with the flow-field visualizations. An increase in rake angle causes the free surface along the side hull to undergo overturning at an earlier stage and generates a stronger jet impingement during the subsequent fallback, leading to a more pronounced secondary impact on the side shell. In contrast, a smaller heel angle promotes water accumulation in the side region. The overturning motion is thereby suppressed, resulting in a reduced secondary impact amplitude. These observations indicate that the rake angle modifies the load distribution on the side hull primarily by altering the timing and intensity of wave overturning, rather than by simply changing the magnitude of the initial wave impact.

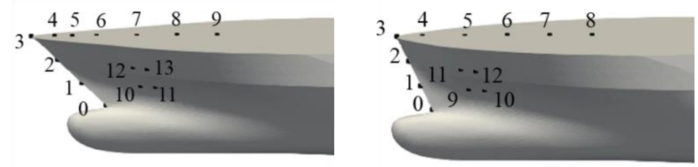

(a) Position of probes in case2 (b) Position of probes in case3

Fig. 17 Position of probes in case2 and case3

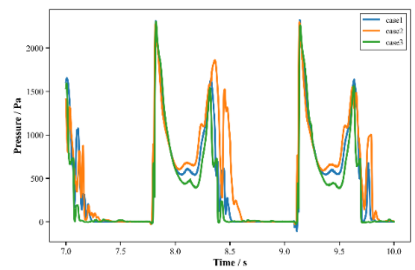

Fig. 18 Time histories of pressure for case 1 (probe 11), case 2 (probe 12) and case 3 (probe 11)

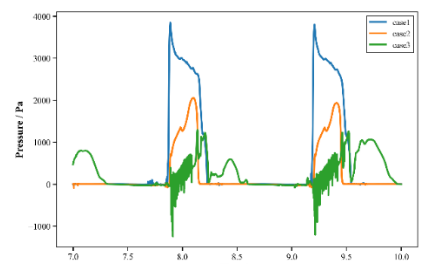

Fig. 19 Time histories of pressure for probe 3 in three cases

Fig. 19 compares the time histories of pressure for probe 3 in three cases. Based on the time histories, a comprehensive interpretation of the curve characteristics for the different cases can be made. In case 1, the pressure record exhibits narrow and high peaks, indicating that the probe is subjected to a direct and concentrated jet or liquid-column impact. After the impact, the probe remains covered by a layer of residual water. As a result, the pressure decays gradually rather than dropping abruptly, until the probe is re-exposed to air. The pressure response in case 2 is characterised by a continued pressure increase following the initial impact, forming a broader high-pressure region. This suggests that after the first contact, the jet continues to develop and delivers additional fluid to the probe location, thereby extending the loading duration. This behaviour is consistent with the earlier overturning and breaking of the bow wave induced by an increased heel angle. The premature breaking leads to a redistribution of the incoming flow before it reaches the probe, reducing the instantaneous impact intensity while producing a more sustained pressure response. In case 3, the pressure signal shows frequent oscillations accompanied by pronounced negative values. This behaviour is likely associated with a reduced bow heel angle, under which the climbing wave advances more slowly onto the deck. The water accumulates locally near the probe and entrains a significant amount of air, resulting in strong pressure fluctuations and intermittent negative pressures. Although the momentum of the incoming water is relatively small, the accumulated water volume is large. When bow-up motion occurs, part of the water is squeezed and driven back toward the bow, flowing off the deck and generating a secondary, smaller pressure peak.

It should also be noted that during the period of strong oscillation, the probe is located close to the instantaneous free surface. Under such conditions, the relatively large negative pressures observed in case 3 may be influenced by numerical oscillations associated with multiphase interface capturing. This issue requires further investigation through refined post-processing or numerical sensitivity studies. In the present work, it is discussed only as a plausible contributing factor.

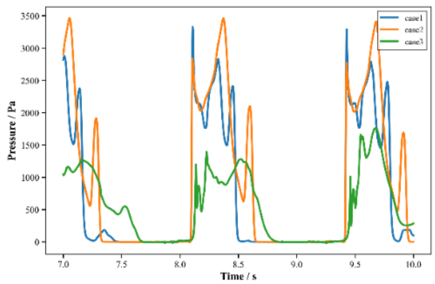

Fig. 20 Time histories of pressure for case 1 (probe 5), case 2 (probe 6) and case 3 (probe 4)

Fig. 20 presents pressure time histories at probes located at the same x position on the forward deck for the three cases. The curves allow a direct comparison of rake angle affects timing, peak magnitude and duration at a representative deck location.

CONCLUSIONS

This paper presents a numerical investigation of green-water on a KCS hull, focusing on the influence of bow rake angle. Regular waves were generated in an HOS domain and coupled to a CFD model of the KCS geometry; three rake configurations were simulated and analysed using free-surface visualisations and a series of pressure probes on the stem, hull sides and fore deck.

The results show that green-water on the KCS follows a reproducible multi-stage sequence — lateral run-up, localized overturning and partial breaking, jetting and tongue formation, a plunging-dam-break (PDB)-type plunging impact on the fore deck, and subsequent pooling and lateral dispersion — and that these stages govern both instantaneous peak pressures and longer-duration impulses. Peak pressures are not confined to the stem tip but concentrate slightly aft of the stem and offset from the centreline on the deck and side hull, consistent with high-momentum jets undergoing strong normal deceleration upon impact. Temporal partitioning is clear: early short impulses arise from side-runup and local convergence; mid-height breaking/jetting produces the strongest transient peaks; deck inundation yields longer-duration high-pressure plateaus whose impulse can equal or exceed short peaks.

Bow rake angle significantly influences the timing and the spatio-temporal distribution of overturning and the resulting loads. Specifically, increasing rake tends to advance the onset of side-hull overturning and promote earlier breaking and jet formation, which increases the magnitude of subsequent secondary impacts on the side shell; decreasing rake delays overturning, permits greater mass accumulation ahead of the bow, and produces larger, longer-lasting tongue-shaped inundations that generate prolonged deck loading and stronger pressure oscillations (including intermittent negative excursions). In other words, rake alters when and how the free surface overturns and thereby redistributes pressures in time and space.

ACKNOWLEDGEMENTS

This work is supported by the National Natural Science Foundation of China (52571359, 52131102), to which the authors are most grateful.

REFERENCES

Boon, A.D. and Wellens, P.R. (2024) “Kinematics of green water in a large data set of events and a resulting prediction method of probability”, *Ocean engineering,* 311, p. 118776.

Dommermuth, D.G. and Yue, D.K.P. (1987) “A high-order spectral method for the study of nonlinear gravity waves”, *Journal of fluid mechanics*, 184, pp. 267–288.

Gatin, I, VUKČEVIĆ V, JASAK H, et al. (2018) “CFD verification and validation of green sea loads”, *Ocean engineering*, 148, pp. 500–515.

Jacobsen, N.G., Fuhrman, D.R. and Fredsøe, J. (2012) “A wave generation toolbox for the open-source CFD library: OpenFoam”, *International journal for numerical methods in fluids*, 70(9), pp. 1073–1088.

Jiao, J. Huang S, Tezdogan T, et al. (2021) “Slamming and green water loads on a ship sailing in regular waves predicted by a coupled CFD–FEA approach”, *Ocean engineering*, 241, p. 110107.

Kudupudi, R.B., Datta, R. and Guedes Soares, C. (2023) “Modelling green water loads on ships using coupled impulse response function and CFD solution”, *Ocean engineering*, 281, p. 114918.

LARSSON L, STERN F, VISONNEAU M, et al. (2015) Proceedings, Tokyo 2015 Workshop on CFD in Ship Hydrodynamics.

LE TOUZÉ D, MARSH A, OGER G. et al. (2010) “SPH simulation of green water and ship flooding scenarios”, *Journal of hydrodynamics*. Series B, 22(5), pp. 231–236.

Lee, H.-H., Lim, H.-J. and Rhee, S.H. (2012) “Experimental investigation of green water on deck for a CFD validation database”, *Ocean engineering*, 42, pp. 47–60.

Liu, D., Li, F. and Liang, X. (2022) “Numerical study on green water and slamming loads of ship advancing in freaking wave”, *Ocean engineering*, 261, p. 111768.

Shen, Z, and Wan, DC (2016) “An Irregular Wave Generating Approach Based on naoe-FOAM-SJTU Solver”, China ocean engineering, 30(2), pp. 177 – 192.

SPALART P R, DECK S, SHUR M L, et al. (2006) “A new version of detached-eddy simulation, resistant to ambiguous grid densities”. Theoretical and Computational Fluid Dynamics, 20(3): 181-195

West, B.J. et al. (1987) “A new numerical method for surface hydrodynamics”, *Journal of Geophysical Research*, Wash., D.C, 92(C11), pp. 11803–11824.

Zakharov, V.E. (1972) “Stability of periodic waves of finite amplitude on the surface of a deep fluid”, *Journal of applied mechanics and technical physics*, 9(2), pp. 190–194.

Zhang, C，Zhang W, Qin H, et al. (2023) “Numerical Study on the Green-Water Loads and Structural Responses of Ship Bow Structures Caused by Freak Waves”, *Applied sciences*, 13(11), p. 6791.

Zhuang, Y. and Wan, D. (2021) “Parametric study of a new HOS-CFD coupling method”, *Journal of hydrodynamics*. Series B, 33(1), pp. 43–54